

Efficient Pneumatic Twisted-and-Coiled Actuators Through Dual Enforced Anisotropy

Eric Weissman^{ID}, Brianna Ashcroft, Phong Nguyen, and Jiefeng Sun^{ID}, Member, IEEE

Abstract—The Cavatappi muscle is a novel soft actuator offering many desirable attributes, such as large linear contraction with negligible radial expansion, compliance, and low cost. However, it has a low energy efficiency (9%) and requires high-pressure inputs (over 240 psi), limiting its effectiveness in robotics applications. This work proposes a fiber-reinforced pneumatic twisted-and-coiled actuator (FR-PTCA) that addresses these shortcomings by introducing a fiber reinforcement to increase the tube anisotropy. The FR-PTCA has higher energy efficiency (over 19%) and lower pressure actuation compared to the Cavatappi muscle without sacrificing muscle strain (70% strain at 130 psi). In addition, this work also presents an analytical model of the FR-PTCA that can be used for design optimization and model-based control. The potential applications of these novel actuators are demonstrated through a continuum robot driven by the FR-PTCA.

Index Terms—Continuum robot, fiber reinforced, pneumatic actuator, soft robotics, twisted and coiled actuator.

I. INTRODUCTION

A CTUATORS are essential components in robotics, and soft actuators, often referred to as artificial muscles, are a rapidly growing field of research. An ideal soft actuator should be compliant, controllable, inexpensive, energy-efficient, and exhibit a high work-density ratio [1], [2].

Twisted-and-coiled actuators (TCAs) possess many of the desired traits: low cost, as they can be made from common household fibers (e.g., sewing threads or fishing line); high work density (27.1 kW/kg); and compliance [3], [4], [5]. However, TCAs are limited by low energy efficiencies and slow response times due to thermal activation, constraining their use in high-frequency or untethered robotic applications. To address the weaknesses of the TCA, a fluid-driven TCA was developed—called the Cavatappi muscle due to its Cavatappi-like shape [6]. The Cavatappi muscle operates similarly to the TCA but uses

Received 21 December 2024; revised 21 March 2025; accepted 6 May 2025. Recommended by Technical Editor G. Berselli and Senior Editor Z. Sun. This work was supported by the Ira A. Fulton Schools of Engineering at Arizona State University. (Corresponding author: Jiefeng Sun.)

The authors are with the School for Engineering of Matter, Transport and Energy, Arizona State University, Tempe, AZ 85281 USA (e-mail: eweissm1@asu.edu; bgashcro@asu.edu; nnnguye94@asu.edu; jiefeng.sun@asu.edu).

This article has supplementary material provided by the authors and color versions of one or more figures available at <https://doi.org/10.1109/TMECH.2025.3568353>.

Digital Object Identifier 10.1109/TMECH.2025.3568353

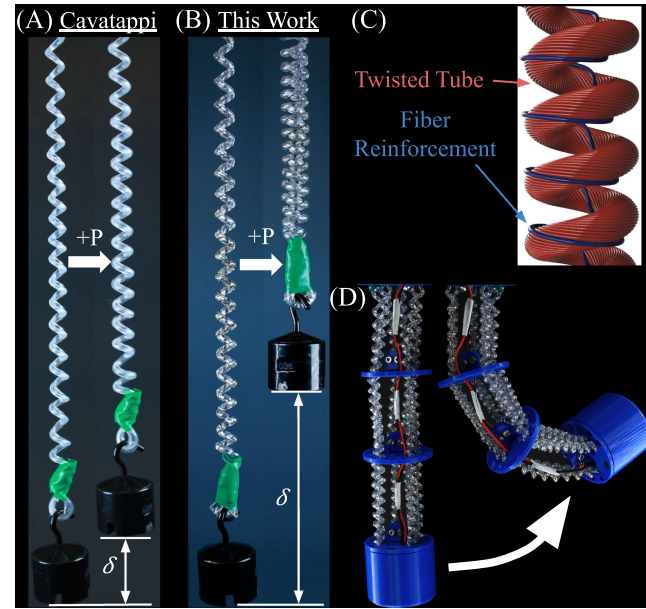


Fig. 1. (a) Cavatappi muscle before (left) and after (right) pressure (130 psi) is applied undergoing displacement δ . (b) FR-PTCA before (left) and after (right) pressure (130 psi) is applied undergoing over twice as much displacement compared with (b). (c) Schematic of the FR-PTCA showing the FR (blue) and the polymer chain reinforced tube with the polymer fibers orientation (red). (d) FR-PTCA driven continuum robot. Video is available online: <https://youtu.be/fIU39fBoMc>

pressurized fluid (e.g., pneumatic) to induce radial expansion, circumventing the limitations of thermal activation.

Compared to traditional pneumatic actuators, such as the McKibben muscle [7] and the pleated pneumatic artificial muscles (PPAMs) [8], [9], [10], Cavatappi muscles [see Fig. 1(a)] have a high energy efficiency (no fiber friction) and can be deployed in parallel as they do not exhibit a large radial expansion [6], [7]. However, Cavatappi muscles require pressures of up to 240 psi to achieve comparable strains (50%) and exhibit low efficiencies (9%) [6], which limits their use in untethered robotics [11] and increases their costs due to the necessity for expensive high-pressure equipment.

In this work, we introduce a novel design that addresses the shortcomings of the Cavatappi muscle by introducing a fiber reinforcement (FR) to enforce the tube anisotropy. We call the new design the fiber-reinforced pneumatic twisted-and-coiled actuator (FR-PTCA) [see Fig. 1(b)] to distinguish it from the Cavatappi muscle. The actuators are created by first wrapping a reinforcement fiber on a cold drawn tube (FR), twisting the tube,

TABLE I
COMPARISON OF FR-PTCA WITH OTHER ACTUATORS AND HUMAN MUSCLE

Actuator	Efficiency* (%)	Max strain (%)	Input pressure (psi)	Response time (ms)	Max stress (MPa)
This work	19.28	70	115	90	0.72
Cavatappi [6]	9	50	240	242	0.7
PPAM [8], [9], [10]	5	38	22	50 to 200	0.67
TCA [4], [5], [13]	1	49	N/A	>1000	38
Fiber reinforced [14]	N/A	15	9	N/A	N/A
Human muscle [13], [15], [16]	40	40	N/A	~ 120	0.35

* Actuator efficiency is defined in terms of unidirectional energy input and output, where recovery is not considered.

and then coiling the tube into a helical shape. Once pressurized, the actuator will linearly contract due to torsional strain in the cold drawn tubes. Since the Cavatappi does not include FR, the muscle's torsional strain (the source of the linear actuation) derives solely from the aligned high-stiffness polymer chain [12]. However, the FR-PTCA derives its anisotropy from the FR and the polymer chain [see Fig. 1(c)], which is the reason behind the higher energy efficiency and lower actuation pressure.

The major contributions of this work are: 1) a novel low-cost soft actuator that has higher energy efficiency (19.28%) and higher strains (up to 70%) for any given input pressure compared to the state-of-the-art muscles, such as the Cavatappi (see Table I), 2) an accurate analytical model of the FR-PTCA, and 3) we demonstrate that the FR-PTCA can replace tendons to enable a controllable, inexpensive continuum robot [see Fig. 1(d)].

The rest of this article is organized as follows. Section II describes the working principles and fabrication methods. Section III provides a comprehensive description of the analytical modeling methods. Section IV presents the muscle characterization and a discussion. Section V demonstrates a robotics application of the FR-PTCA. Finally, Section VI concludes this article.

II. DESIGN AND FABRICATION

In this section, we will first introduce the fabrication process and the key features of the FR-PTCA. We will then analyze why adding the FR increases performance.

A. Fabrication

The fabrication of the FR-PTCA [see Fig. 2] involves the following steps: (I) inserting the core, (II) cold drawing, (III) fiber reinforcing, (IV) twisting, (V) coiling, and (VI) annealing. Described below are the parameters used for the best performing muscle.

I. *Inserting the core:* A thermoplastic polyurethane (TPU) core (1.75 mm PolyFlex TPU95-HF filament) is inserted into an undrawn polyvinyl chloride (PVC) tube (5/32" OD \times 3/32"ID, ND-100-65 Tygon) and one end of the tube is clamped to the core to prevent sliding.

II. *Cold drawing:* The tube is stretched, sliding along the nylon core, by a cold draw ratio $\omega = L_t / L_{\text{init}} = 2.5$, where L_{init} is the initial tube length and L_t is the length after cold drawing. While the FR alone produces anisotropy, the cold drawing can help to further increase anisotropy and reduce the tube's wall thickness. For

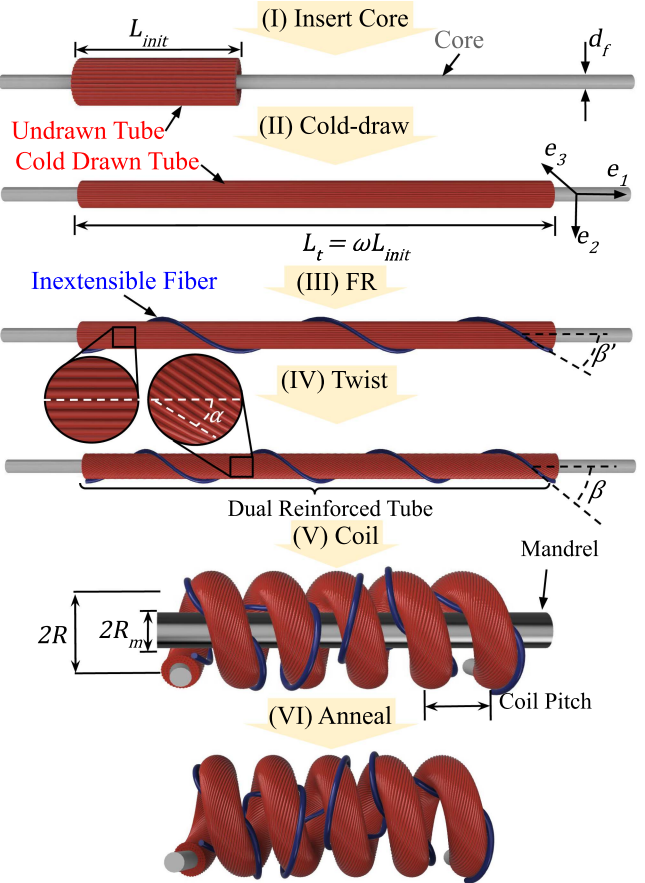


Fig. 2. Fabrication procedures of the FR-PTCA.

any $\omega \leq 3$, we observed no systematic failures during fabrication.

III. *Fiber reinforcing:* A thin nylon monofilament fiber (0.017", Malin Company) is wrapped around the cold drawn tube at a helix angle $\beta' = 35^\circ$ (i.e., a pitch of 12 mm). Tension is maintained in the fiber with a 100 g weight during this step.

IV. *Twisting:* The fiber-reinforced cold drawn tube is twisted with the same chirality as the reinforcing fiber. This results in an angle $\alpha = 15^\circ$ (notated as the twist angle) for the polymer chain in the cold drawn tube and the nylon core. β' increases to $\beta = 40^\circ$, the final FR helix angle. Since the fiber is held in place through friction with the tube, it is recommended to apply the FR before twisting the cold drawn tube. This ensures a tight contact between the reinforcing fiber and the tube, preventing

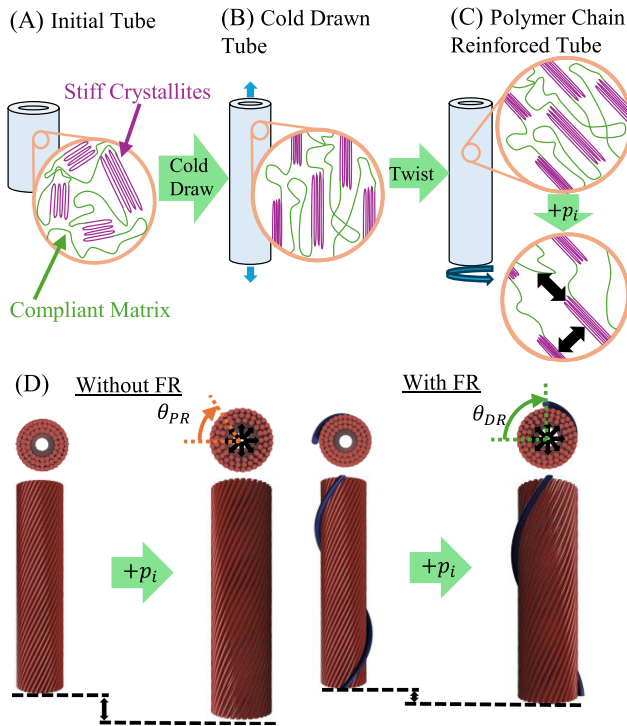


Fig. 3. (a) Undrawn tube with an amorphous polymer structure. (b) Cold drawn tube with stiff crystallites aligned along the drawing direction. (c) Polymer-reinforced tube formed by twisting the cold drawn tube, with polymer chains wrapping helically. Inflation allows crystallites to shift transversely and axially. (d) Schematic showing that adding FR increases untwist.

slippage. The tube after this step is referred to as the dual reinforced tube since the anisotropy is reinforced by both the FR and the high-stiffness polymer chains within the tube.

V. Coiling: The dual reinforced tube is coiled around a mandrel with radius $R_m = 1.5$ mm and a coil pitch of 6 mm, resulting in a mean coil radius of $R = R_m + r_o^*$, where r_o^* is the cold drawn tube's outer radius.

VI. Annealing: With the muscle coiled around the mandrel, it is annealed at 90°C for 45 min, allowing for the core to maintain its coiled form. The finished FR-PTCA is then removed from the mandrel.

B. Working Principle

The Cavatappi is fabricated similarly to the FR-PTCA but excludes the FR step (step III). During cold drawing, the amorphous polymer that initially composes the tube [see Fig. 3(a)] is transformed into a composite material. This material consists of a low-stiffness amorphous polymer matrix and high-stiffness and high aspect ratio crystallites (referred to as polymer chains in this work), oriented along the drawing direction [17] [see Fig. 3(b)]. These aligned polymer chains result in a transversely isotropic material that is stiffer axially than radially. Subsequently, the twisting step aligns the polymer chains into a helical pattern around the tube. The result of these processes is referred to as the polymer chain reinforced tube in this work

[see Fig. 3(c)]. Due to its axial stiffness, the tube untwists when radially expanded by internal pressure, as described by [2] and [4] and the relationship $\theta = (L_t \tan(\alpha))/(2\pi r)$, where α is the helix angle of the polymer chains, r is the radius of the polymer chains, and θ is the twist inserted into the tube. With L_t and α held constant, increasing r decreases θ , resulting in an untwist of the tube. However, it is important to note that this relationship is derived kinematically from the helical geometry of the fiber and assumes that the polymer chains are inextensible.

However, an analysis of the cold drawing process reveals that the assumption of inextensible polymer chains is invalid. Cold drawing does not fully transform the crystalline regions of the tube into aligned polymer chains [17]. Instead, the tube consists of finite-aspect-ratio polymer chains, as described by the Barham and Arridge cold drawing model [18], interspersed within a compliant matrix. Annealing further reduces the aspect ratio of these polymer chains through lamellar thickening [17]. As shown in Fig. 3(c), the finite aspect ratio of the polymer chains allows the compliant matrix to deform in the cold drawing direction when pressure is applied to the tube. Consequently, the previously described kinematic relationship is only partially enforced. This limits the efficiency of energy conversion from radial expansion into untwist. To address this limitation, an FR line is introduced.

The FR significantly increases the tube's anisotropy due to its inextensibility compared to the polymer chain-reinforced tube. For example, the nylon monofilament FR has an axial Young's modulus of 2300 MPa [19] compared to the 61.1 MPa of the cold drawn PVC tube ($\omega = 3$) [2]. This reinforcement restricts axial extension along the polymer chains, confining expansion to the radial direction where the fiber is present and enabling a more efficient energy conversion from radial expansion to untwist of the tube [see Fig. 3(d)].

III. ANALYTICAL MODELING

In this section, we present a precise analytical model to predict the static performance of the FR-PTCA. The models can be used to optimize the FR-PTCA design and improve controller performance. The following assumptions are made: 1) the tube is made of a linear elastic material, 2) the FR is inextensible and does not slip, and 3) the fiber helix angle remains constant throughout actuation.

A. Equilibrium Equations

The objective of the model is to predict the displacement δ of the muscle as a function of actuation force F and internal input pressure p_i [see Fig. 4(a)] at static assumption (no inertial or damping effects). The actuation force is equal to the external force applied, and because the core and the dual reinforced tube are in parallel under F

$$F = F_c + F_t \quad (1)$$

where F_c and F_t are the forces applied to the core and the dual reinforced tube, respectively. Equation (1) can then be rewritten in terms of the displacement $F = k_c \delta + F_t$, where k_c is the linear stiffness of the coiled core. k_c can be modeled using the

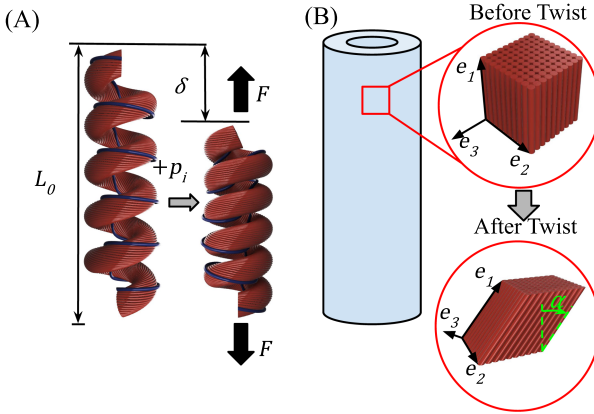


Fig. 4. (a) Schematic of the FR-PTCA actuating. (b) Schematic showing the orientation of the cold drawn tube's polymer fibers before and after twisting.

coiled spring theory presented in [20]

$$k_c = \frac{G_c d_c^4}{8n(2R)^3} \quad (2)$$

where \$G_c\$ is the core's shear modulus, \$d_c\$ is the core's diameter, \$n\$ is the number of coils, and \$R\$ is the mean coil radius, all of which are known geometric/material parameters of the muscle.

To find \$\delta\$ from (1), we next need a function containing \$F_t\$, which can be found from the stress field of the dual reinforced tube. Wahl's [20] coiled spring theory shows \$\varepsilon_a = \delta/L_0 = \gamma_{12} \frac{2\pi n R^2}{r_o L_0}\$, where \$\varepsilon_a\$ is the linear strain of the FR-PTCA, \$r_o\$ is the deformed outer radius of the tube, \$L_0\$ is the initial length of the coiled muscle, and \$\gamma_{12}\$ is the shear strain in the dual reinforced tube around the tube axis [see Fig. 4(b)]. Wahl's relationship can be rearranged as

$$\delta = \gamma_{12} \frac{2\pi n R^2}{r_o}. \quad (3)$$

The radial displacement of the tube due to pressurization can be determined from Lamé's equations for thick-walled pressure vessels [21] as \$r_o = r_o^* + u(r_o^*)\$. The symbol * indicates that the length value corresponds to the unpressurized tube dimensions, and \$u\$ is the tube radial displacement function (defined later) estimating the radial displacement at a radius \$r\$ due to \$p_i\$.

Thus, to solve (3) \$\gamma_{12}\$ is needed. We assume both the FR and the high-stiffness polymer chains as elastic constraints applying a torsional shear on a homogeneous tube: \$\tau = \tau_{\text{FR}} + \tau_{\text{PR}}\$, where \$\tau_{\text{FR}}\$, \$\tau_{\text{PR}}\$, and \$\tau\$, are the torsional shears from the FR, the high-stiffness polymer chains, and the combined shear, respectively. With the assumption of linear material properties, we can apply the principle of superposition to obtain the total strain under input pressure \$p_i\$

$$\gamma_{12} = \gamma_{12}^{\text{FR}} + \gamma_{12}^{\text{PR}} \quad (4)$$

where \$\gamma_{12}^{\text{FR}}\$ and \$\gamma_{12}^{\text{PR}}\$ are the shear strain contributions due to the FR and the high-stiffness polymer chain, respectively, when pressure and external load are applied.

B. Tube Stress Field

\$\gamma_{12}^{\text{PR}}\$ can be found using the analysis provided by [2]. The tube is assumed to be a linear transverse isotropic material with the coordinate frame, as shown in Fig. 4(b). The cold drawn and twisted tube's compliance matrix in Voigt notation is thus \$\bar{S} \in \mathbb{R}^{6 \times 6}\$ (details on the calculation of \$\bar{S}\$ can be found in Supplementary Material 1). The assumption of linear material properties, while not fully accurate for hyperelastic and viscoelastic materials, such as PVC [22], is adequate due to the relatively small changes in stress imparted into the material throughout actuation.

Then, following Hooke's law, \$\varepsilon = \bar{S}\sigma\$, where \$\varepsilon\$ is the strain and \$\sigma\$ is the stress in Voigt notation, the strain–stress relation for the tube can be found

$$\gamma_{12}^{\text{PR}} = (\bar{S}_{61}\sigma_{11} + \bar{S}_{62}\sigma_{22} + \bar{S}_{63}\sigma_{33} + \bar{S}_{66}\sigma_{12}) / 2 \quad (5)$$

where \$\bar{S}_{ij}\$ is the entry from the \$i\$th row and \$j\$th column of \$\bar{S}\$. Subsequently, the normal stresses (\$\sigma_{ij}\$, where \$i = j\$) and the shear stress \$\sigma_{12}\$ are needed in terms of \$F_t\$ and \$p_i\$.

The normal stresses \$\sigma_{ij}\$ and the tube displacement function \$u\$ can be obtained from Lamé's equations for a thick-walled vessel with pressure \$p_i\$ [21]

$$\sigma_{11} = A, \sigma_{22} = A - B, \sigma_{33} = A + B \quad (6)$$

$$u(r) = \frac{1 - \nu_{23}}{E_2} A^* r + \frac{1 + \nu_{23}}{E_2} B^* \frac{r_o^*}{r}$$

where \$A = \frac{r_i^2 p_i - r_o^2 p_{\text{atm}}}{(r_o^2 - r_i^2)}\$, \$B = \frac{(p_i - p_{\text{atm}})r_i^2}{(r_o^2 - r_i^2)}\$, \$r_i = r_i^* + u(r_i^*)\$ is the inner radii of the pressurized tube, \$p_{\text{atm}}\$ is the atmospheric pressure, \$E_i\$ is the Young's modulus, \$G_{ij}\$ is the shear modulus, \$\nu_{ij}\$ is the Poisson's ratio, and \$i, j = 1, 2, 3\$ are corresponding to the material frame axes \$(e_1, e_2, e_3)\$, respectively.

Next, to find \$\gamma_{12}^{\text{PR}}\$ we need to determine \$\sigma_{12}\$. Again using Wahl's spring theory [20], the loading and curvature effects on the coiled tube give

$$\sigma_{12} = F_t \Lambda \quad (7)$$

where \$\Lambda = (\pi(r_o^2 - r_i^2))^{-1} - \frac{4R^2 r_o (4R + r_o)}{\pi(8R^2 + 8Rr_o + r_o^2)(r_o^4 - r_i^4)}\$. Thus, by substituting (6) and (7) into (5), we can calculate \$\gamma_{12}^{\text{PR}}\$ with \$p_i\$ and \$F_t\$.

C. FR Effects

The next step in finding \$\gamma_{12}\$ is to find \$\gamma_{12}^{\text{FR}}\$. As shown by Krishnan [23], the untwist from the FR of a tube during inflation can be modeled kinematically by assuming the fiber to be inextensible and \$\beta\$ constant

$$1 = (1 + \varepsilon_{11})^2 \cos(\beta)^2 + \left(\frac{r_o}{r_o^*}\right)^2 \sin(\beta)^2 \left(1 + \frac{\theta_{\text{FR}} r_o}{L_t \tan(\beta)}\right)^2 \quad (8)$$

where \$\varepsilon_{11}\$ is the axial strain of the tube and \$\theta_{\text{FR}}\$ is the untwist angle of the tube. Given the definition of torsional shear strain on the surface of a tube, \$\gamma_{12}^{\text{FR}} = (\theta_{\text{FR}} r_o)/L_t\$, and noting that

$\varepsilon_{11} \ll 1$, we can rearrange (8) to find γ_{12}^{FR}

$$\gamma_{12}^{\text{FR}} = \tan(\beta) \left(\sqrt{\frac{1 - \cos(\beta)^2}{\frac{r_o}{r_o} \sin(\beta)^2}} - 1 \right). \quad (9)$$

D. Final Displacement Model

Equations (4), (5), and (9) can be used to calculate γ_{12} , which can then be combined with (1)–(3) to solve for the δ in terms of F , p_i , and known geometric/material parameters

$$\delta = \frac{\varphi (\psi + F \Lambda \bar{S}_{66} + 2\gamma_{12}^{\text{FR}})}{2 + \Lambda \varphi k_c \bar{S}_{66}} \quad (10)$$

where $\varphi = \frac{2\pi n R^2}{r_o}$ and $\psi = \bar{S}_{61}\sigma_{11} + \bar{S}_{62}\sigma_{22} + \bar{S}_{63}\sigma_{33}$. φ , ψ , γ_{12}^{FR} , and Λ are all functions of p_i and known geometric/material parameters. To employ the model, measurements of the cold drawn tube's inner and outer radii, the length of the coiled muscle, the number of coils, the coil mean radius, the core diameter, the twist angle of the tube, and the FR helix angles are needed. In addition, the orthotropic material properties of the cold drawn tube are required [2]. Then, for any input pressure and applied force, the displacement of the muscle can be found with (10) so long as the assumption of linear material properties remains valid. Model parameters for the muscle described later in Section IV-B are as follows: $r_o^* = 1.3$ mm, $r_o^* = 0.59$ mm, $R_m = 3$ mm, $\alpha = 21^\circ$, $\beta = 46^\circ$, $d_c = 1.1$ mm, $G_c = 540$ MPa, and $n = 20$.

IV. CHARACTERIZATION AND MODEL VALIDATION

In this section, we experimentally characterize the FR-PTCA's performance and validate the proposed model.

A. Untwist From FR

To validate that FR results in additional untwist of the dual reinforced tube, we began by measuring the untwist versus input pressure for a polymer chain reinforced and a dual reinforced tube [see Fig. 5(a)]. The tubes were constructed with the following parameters: 5/32" × 3/32" ND-100-65 Tygon PVC tube, a 0.043" nylon monofilament filament core (Malin company), $\omega = 3$, $\beta = 46^\circ$ (for the dual reinforced tube), $\alpha = 20^\circ$, and $L_t = 20$ cm. Pressure was supplied through a pressure regulator with a built-in pressure sensor (Festo VEAA-L-3-D11-Q4-V2-1R1) and the twisting motion was recorded as a video and analyzed using Tracker software (Physlets). The regulator was controlled via an Arduino Mega microcontroller, which ramped the pressure over 60 s to the maximum pressure of 80 psi. In this work, the solid line represents the average of three trials and the shaded area represents the standard deviation. The results show that the introduction of FR increases the untwist of the tube by three times at 80 psi compared to the Cavatappi.

B. Experimental Setup and Procedures

In this section, we introduce the characterization setup used for Sections IV-C, IV-D, and V-A [see Fig. 5(b)]. An FR-PTCA is hung with a weight at the end. We use the same pressure

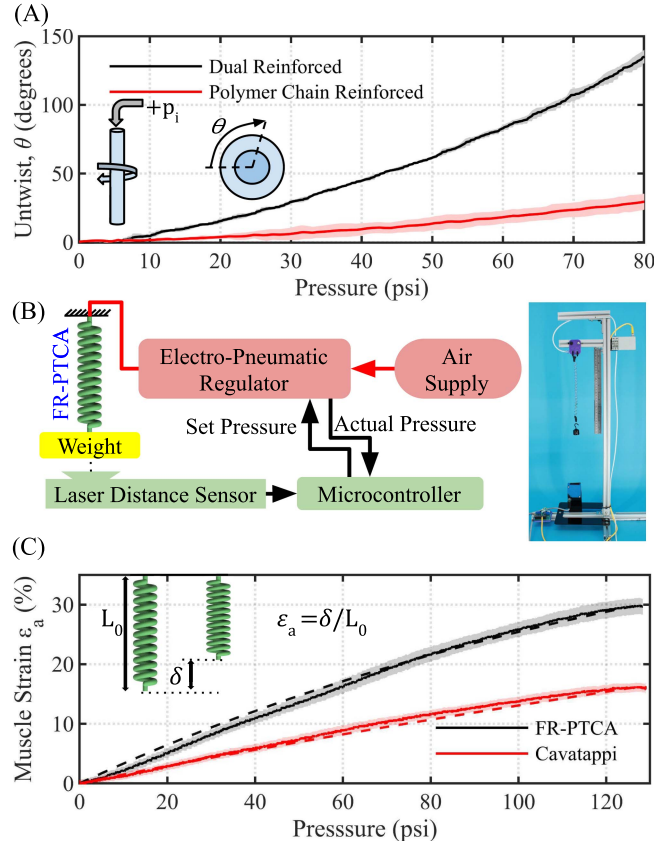


Fig. 5. (a) Comparison between the polymer chain and dual reinforced tubes analyzing the untwist due to internal pressure. (b) Experimental setup for Sections IV-C, IV-D, and V-A. (C) Comparison between the Cavatappi and FR-PTCA muscles analyzing muscle strain due to internal pressure. Dashed lines show results predicted by the model.

regulator used in Section IV-A to control the pressure supplied to the FR-PTCA, and a laser distance sensor (Wenglor OPT2006) to measure the displacement of the muscle. They both are connected to an Arduino Mega microcontroller for control and data acquisition.

To analyze the muscle performance and to validate the accuracy of the model over a variety of muscle designs, this study analyzed orthogonal slices of the design space, all intersecting at a default muscle (i.e., each muscle was a one variable permutation of the default muscle). This default muscle has the following design parameters: 5/32" × 3/32" ND-100-65 Tygon PVC tube with $\omega = 3$, $\beta = 46^\circ$, $\alpha = 21^\circ$, and $R_m = 1.5$ mm, and the coil pitch equal to 6 mm. A 0.043" Malin company nylon monofilament line was selected as the core for this default muscle [6]. Each test was performed with a 100 g load on the muscle and three trials were conducted for each experiment. Finally, the anisotropic PVC material properties found in [2] are used in the model.

C. FR-PTCA Model Validation and Muscle Performance

To verify that the increased untwist observed in Section IV-A improves coiled muscle performance, we constructed an FR-PTCA and a Cavatappi with identical parameters. Fig. 5(c) shows that FR increases strain at a given pressure—e.g., 29.8%

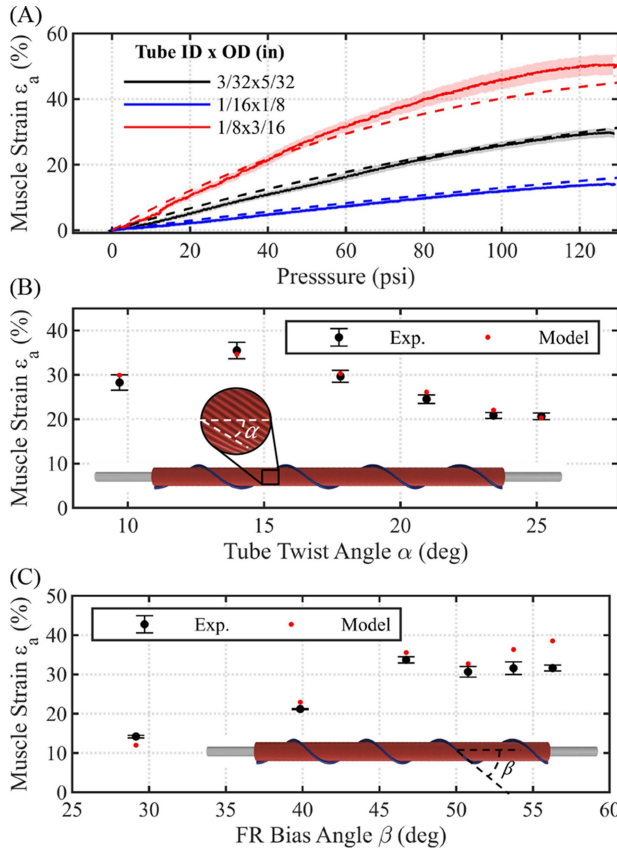


Fig. 6. Experimental (solid lines) and model predicted (dashed lines) strains for the FR-PTCA over a range of (a) tube geometries, (b) tube twist angles at 130 psi, and (c) FR bias angle at 130 psi.

strain at 130 psi compared to 15.2% for the Cavatappi. In addition, the model accurately predicts strain for both muscles, with a maximum error of 1.3%.

The Cavatappi exhibited 14.83% hysteresis, defined as $100 \times \frac{\Delta\epsilon}{\max(\epsilon)}$, where $\Delta\epsilon$ is the peak difference between the forward and reverse trajectory. The FR-PTCA exhibited slightly higher hysteresis at 19.66%, likely due to increased fiber-tube friction, similar to McKibben muscles [7]. For clarity, only the forward trajectory is plotted in Fig. 5(c) and subsequent figures.

Next, we assess the model's performance across varying tube geometries. Fig. 6(a) illustrates the results for varying the tube diameter. With constant wall thickness, increasing the tube radius leads to greater muscle strain at a given pressure due to higher hoop stress and greater radial expansion. However, as noted in [6], this performance increase must be balanced against the muscle's rupture pressure, as larger tubes are more prone to failure or reduced lifespan at elevated pressures. The model effectively predicts strain for smaller tubes, but its accuracy diminishes for larger tubes at higher pressures due to significant nonlinear material effects, such as hyperelasticity, which the model assumes negligible.

Fig. 6(b) shows the strain achieved by the FR-PTCA at 130 psi as the twist angle α varies. The results reveal an optimal twist angle around 14° with the model accurately predicting the strain across this range. Similarly, Fig. 6(c) presents the strain at

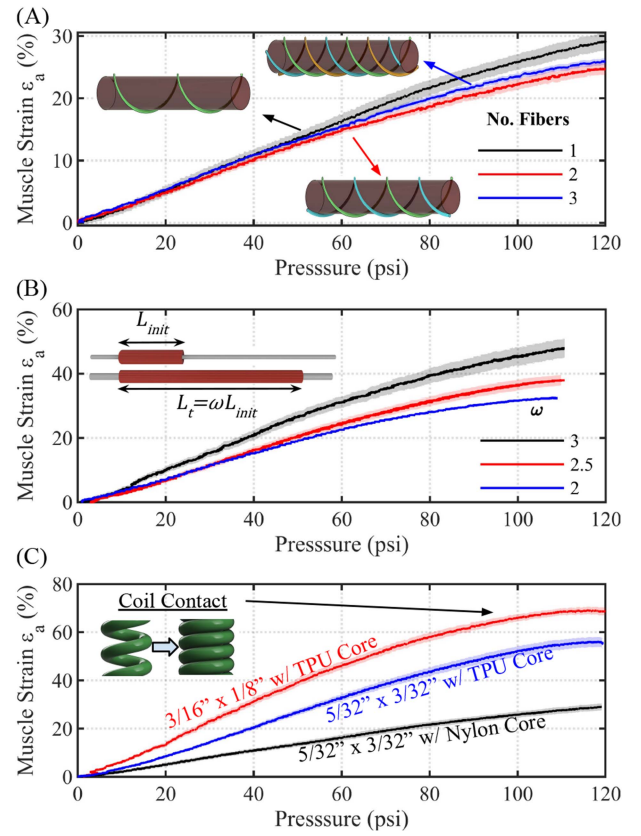


Fig. 7. Effect on strain versus pressure for (a) different numbers of fibers, (b) various cold draw ratios, and (c) various core materials.

130 psi as the FR helix angle β is varied. The data indicate an optimal helix angle near 46° and that the model is capable of accurately predicting the strains for small β angles. However, for larger helix angles, the model overpredicts strain due to the tube ballooning where the FR is not present [23], which reduces the shear force generated by the FR. These results demonstrate that the model reliably predicts muscle performance within a bounded parameter domain. Note that model validation and a discussion on the effect of varying the load on the FR-PTCA is shown in Supplementary Material 3.

D. FR-PTCA Design Parameters and Consideration

To provide insights on selecting design parameters for the FR-PTCA, we analyze three key questions: 1) is using multiple reinforcement fibers optimal, 2) how should the cold draw ratio be selected, and 3) how does the core diameter and material impact the muscle's performance?

For the first question, Fig. 7(a) shows strain versus pressure curves for the FR-PTCA with one, two, and three FR families. A single fiber outperforms configurations with multiple fibers. Meanwhile, there is only a 1.3% difference in performance between two and three fibers. This could be because additional fibers do not increase the torsional shear strain within the FR-PTCA tube. Instead, they restrict radial expansion resulting in reduced performance with additional fibers.

The selection of the cold draw ratio requires balancing lifespan and performance. As shown in Fig. 7(b), strain increases with the cold draw ratio at a given pressure due to higher tube anisotropy and wall thinning. However, anecdotal observations indicate that higher ratios also shorten the muscle's lifespan (i.e., the number of cycles at the maximum operational pressure before rupture) due to increased damage accumulation [24]. We observed that at $\omega = 3$, the muscle survived 34 cycles at 120 psi before failing. Meanwhile, at $\omega = 2.5$, the muscle survived 120 cycles at 130 psi before failure and more than 1000 cycles when actuated at 100 psi. Future work will analyze quantitatively this relationship between ω and the muscle lifespan. Nevertheless, in Section V, a ratio of $\omega = 2.5$ is selected to balance high performance with improved lifespan.

Answering the third question of how a core is selected, there are two factors to consider: material selection and core diameter. Our testing suggests that the core diameter for practical applications of the muscle should be the largest that fits within the cold drawn tube. Undersized cores lead to the tube kinking during the twisting step or flattening against the mandrel during annealing. These geometric features introduce gradients within the tube's stress field, causing premature failures of the tube at these features. For the core material, Fig. 7(c) shows that materials with lower shear moduli, such as TPU 95 A, achieve much higher strains compared to stiffer materials, such as nylon monofilament. For example, with the same $3/16'' \times 1/8''$ tube, a TPU core achieved a strain of 70% at 115 psi, compared to 28.5% for the nylon core. However, TPU cores also reduce muscle stiffness, increasing compliance (0.164 N/cm versus 0.245 N/cm for a nylon-core muscle). Thus, TPU cores are preferred unless higher stiffness is required.

Finally, energy efficiency η was characterized (see Supplementary Material 2 for details). The TPU-core muscle with a $3/16'' \times 1/8''$ tube [see Fig. 7(c)] achieved peak energy efficiencies of 6.8% and 19.28% at 130 psi under 100 and 200 g loads, respectively. However, there was coil contact during the 100 g load for the muscles, meaning the measured work output was skewed.

V. CONTROL AND CONTINUUM ROBOT APPLICATION

A. Closed-Loop Position Control

To assess the FR-PTCA's suitability for robotic applications, we analyzed its dynamic response and dead band from a 100 psi pressure step input. Both the FR-PTCA and the Cavatappi muscle were fabricated with identical lengths ($L_t = 300$ mm) and tested under the conditions outlined in Section IV-B.

As shown in Fig. 8(a), both actuators exhibit a 118 ms dead band between pressure change detection (sensor located at the muscle inlet) and motion onset, due to viscous air flow through the gap between the tube and core, as observed in [2]. This delay depends on tube-core radius differences, muscle length, and input pressure magnitude. In addition, the FR-PTCA showed an average speed of 77.7% strain/s during the initial rise.

To evaluate controllability, we implemented two closed-loop controllers to track a 1 Hz sinusoidal reference [see Fig. 8(b)].

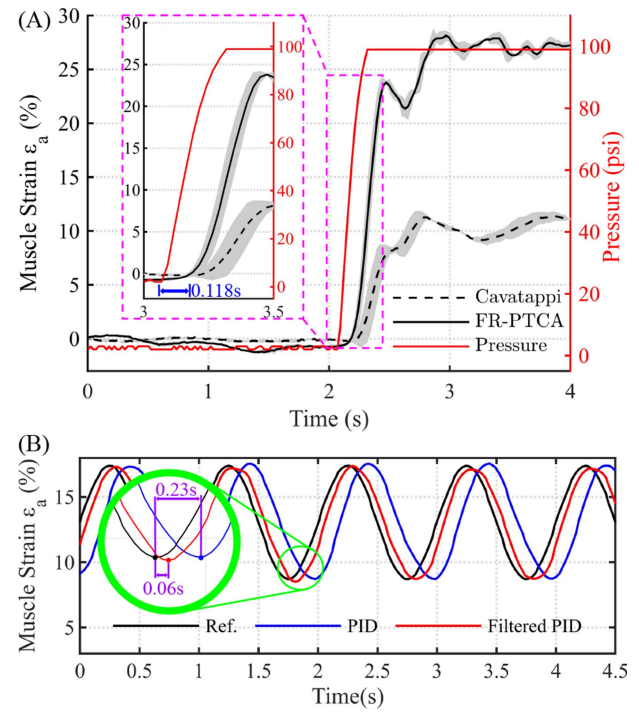


Fig. 8. (a) Pressure step response of the FR-PTCA and Cavatappi with a 100 g load. (b) Demonstration of using the FR-PTCA to track a 1 Hz sinusoidal reference signal with PID and all-pass filtered PID controllers.

A proportional–integral–derivative (PID) controller accurately maintained amplitude and shape but lagged by 230 ms due to transport delay, hysteresis, and the regulator response. Applying an all-pass filter [25] reduced this lag to 60 ms, demonstrating that, despite transport delay, the FR-PTCA enables rapid and precise control, making it well-suited for dynamic robotic applications.

B. Continuum Robot

To validate practical integration, we developed a single-stage continuum robot actuated by FR-PTCAs [see Figs. 1(d) and 9(A)]. Traditional continuum robots rely on bulky, expensive, and mechanically complex tendon systems [26], whereas FR-PTCAs offer a more compact and cost-effective alternative. The robot employed three muscle pairs, each controlled by an electro-pneumatic pressure regulator (Festo VEAA-L-3-D11-Q4-V2-1R1). A NiTi backbone (180 mm × 0.8 mm) provided structural support, and a laser diode at the end effector enabled positional tracking. No payload was present on the robot.

We controlled the continuum robot with a similar strategy, as shown in Section V-A. The robot was mounted above a semitranslucent screen [see Fig. 9(b)], with the laser diode projected onto said screen. A camera mounted below tracked the laser's position as feedback for the end effector. We designed a controller to command the robot to track periodic trajectories in polar coordinates, defined by the trajectory radius r_{tr} and the angle ϕ_{tr} . The control strategy employed two orthogonal PI controllers to minimize the radial error $e_r = r_{tr} - r_L$ and

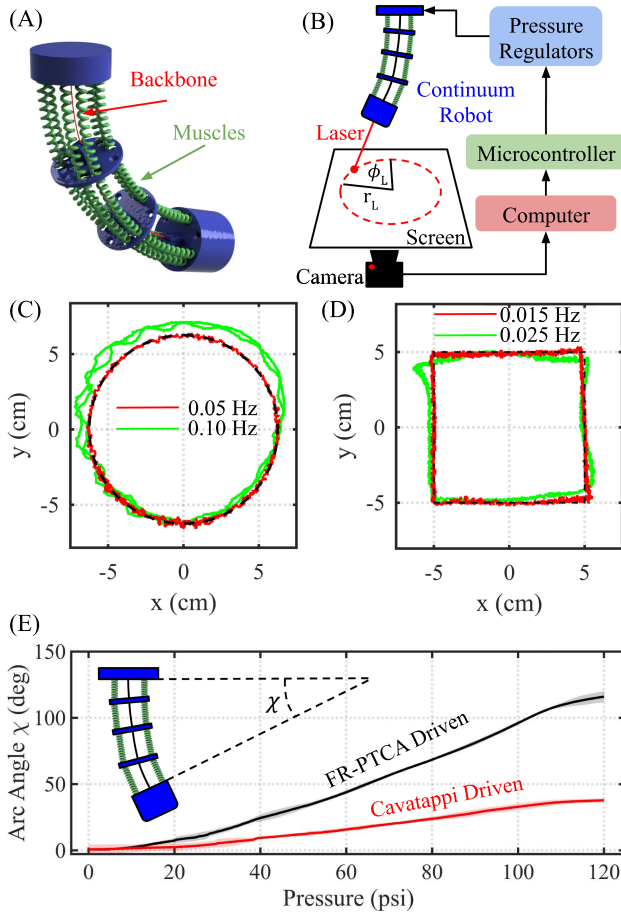


Fig. 9. (a) Continuum robot design with a trisymmetric muscle layout. (b) Schematic of the experimental setup for closed-loop control. (c) and (d) Tracked trajectories of the robot following circular and rectangular paths, with the reference trajectory shown as a dashed line. (e) Backbone arc angle comparison between FR-PTCA and Cavatappi-driven continuum robots.

angular error $e_\phi = \phi_{tr} - \phi_L$, where r_L and ϕ_L are the actual polar coordinates of the laser. The periodic nature of the trajectories allowed for parameterization of the pressure input to each muscle group using time t and the trajectory's frequency f . The control law is expressed as

$$P_j = \left(K e_r + I \int e_r \right) \sin \left(2\pi f t + \phi_{o,j} + K_\phi e_\phi + I_\phi \int e_\phi \right) \quad (11)$$

where P_j is the pressure of muscle group $j \in \{1, 2, 3\}$, $\phi_{o,j} \in \{0^\circ, 120^\circ, 240^\circ\}$ is the phase offset for each muscle group, and K, I, K_ϕ and, I_ϕ are controller gains.

The FR-PTCA robot successfully followed circular and square trajectories [see Fig. 9(c) and (d)]. At 0.05 Hz, the circular trajectory had a maximum error of 3.8 ± 0.7 mm, while at 0.015 Hz, the square trajectory error was 5.2 ± 0.7 mm. The performance drop at higher frequencies is attributed to the limitations of the controller. While more advanced controllers [26], [27] could improve the bandwidth and precision of the continuum robot control, this analysis demonstrated that the FR-PTCA can leverage simple PI controllers to produce controllable robotic systems.

To compare FR-PTCAs with Cavatappi actuators, we constructed an identical continuum robot using Cavatappi muscles. As shown in Fig. 9(e), the FR-PTCA robot achieved a significantly greater backbone arc χ , reaching 114° at 120 psi, compared to 38° for the Cavatappi-driven robot. These results demonstrate the practical advantages of FR-PTCAs, highlighting its potential to enhance the workspace, efficiency, and mechanical simplicity of soft robotic systems.

VI. CONCLUSION

This article introduces and models the FR-PTCA, a low-cost, fluid-driven actuator achieving high strains (70%) at reduced pressures (115–130 psi). By incorporating FR, it enhances efficiency and actuation performance over TCAs and Cavatappi muscles. Experimental validation demonstrates a 19% efficiency, and confirms the accuracy of the analytical model across various design parameters. Future work should integrate self-sensing capabilities, as demonstrated in [28], to enable real-time feedback and closed-loop control, minimizing reliance on external sensors. Further studies should also quantify the effects of fiber angle, core material, and cold-draw ratio on hysteresis, lifespan, and force output to enhance long-term reliability in soft robotics. In addition, exploring new robotic applications will provide practical insights into the use of the FR-PTCA.

REFERENCES

- [1] G. M. Whitesides, "Soft robotics," *Angewandte Chemie (Int. ed.)*, vol. 57, no. 16, pp. 4258–4273, 2018.
- [2] D. R. Higueras-Ruiz, H. P. Feigenbaum, and M. W. Shafer, "Material-based modeling of Cavatappi artificial muscles," *Smart Mater. Struct.*, vol. 31, Nov. 2022, Art. no. 125021.
- [3] A. M. Swartz, D. R. H. Ruiz, H. P. Feigenbaum, M. W. Shafer, and C. C. Browder, "Experimental characterization and model predictions for twisted polymer actuators in free torsion," *Smart Mater. Struct.*, vol. 27, no. 11, 2018, Art. no. 114002.
- [4] C. S. Haines et al., "Artificial muscles from fishing line and sewing thread," *Science*, vol. 343, no. 6173, pp. 868–872, 2014.
- [5] A. Gonzalez-Vazquez, L. García, and J. Kilby, "Improved performance in temperature and speed of TCP artificial muscles for soft wearables robots by length modification," *Smart Mater. Struct.*, vol. 32, no. 8, 2023, Art. no. 85002.
- [6] D. R. Higueras-Ruiz, M. W. Shafer, and H. P. Feigenbaum, "Cavatappi artificial muscles from drawing, twisting, and coiling polymer tubes," *Sci. Robot.*, vol. 6, no. 53, 2021, Art. no. eabd5383.
- [7] R. V. Ham, T. G. Sugar, B. Vanderborght, K. W. Hollander, and D. Lefebvre, "Compliant actuator designs," *IEEE Robot. Automat. Mag.*, vol. 16, no. 3, pp. 81–94, Sep. 2009.
- [8] F. Daerden, D. Lefebvre, B. Verrelst, and R. Van Ham, "Pleated pneumatic artificial muscles: Compliant robotic actuators," in *Proc. IEEE/RSJ Int. Conf. Intell. Robots Syst. Expanding Societal Role Robot. Next Millennium*, 2001, vol. 4, pp. 1958–1963.
- [9] D. Villegas, M. Van Damme, B. Vanderborght, P. Beyl, and D. Lefebvre, "Third-generation pleated pneumatic artificial muscles for robotic applications: Development and comparison with McKibben muscle," *Adv. Robot.*, vol. 26, no. 11–12, pp. 1205–1227, 2012.
- [10] M. Meller, J. Chipka, A. Volkov, M. Bryant, and E. Garcia, "Improving actuation efficiency through variable recruitment hydraulic mckibben muscles: Modeling, orderly recruitment control, and experiments," *Bioinspiration Biomimetics*, vol. 11, no. 6, 2016, Art. no. 065004.
- [11] Y. Jung, K. Kwon, J. Lee, and S. H. Ko, "Untethered soft actuators for soft standalone robotics," *Nat. Commun.*, vol. 15, no. 1, pp. 3510–3510, 2024.
- [12] A. Peterlin, "Plastic deformation and structure of extruded polymer solids," *Polym. Eng. Sci.*, vol. 14, no. 9, pp. 627–632, 1974.
- [13] S. M. Mirvakili and I. W. Hunter, "Artificial muscles: Mechanisms, applications, and challenges," *Adv. Mater.*, vol. 30, no. 6, 2018, Art. no. 1704407.

- [14] F. Connolly, P. Polygerinos, C. J. Walsh, and K. Bertoldi, "Mechanical programming of soft actuators by varying fiber angle," *Soft Robot.*, vol. 2, no. 1, pp. 26–32, 2015.
- [15] D. Sutton and J. Kimm, "Reaction time of motor units in biceps and triceps," *Exp. Neurol.*, vol. 23, no. 4, pp. 503–515, 1969.
- [16] J. D. W. Madden et al., "Artificial muscle technology: Physical principles and naval prospects," *IEEE J. Ocean. Eng.*, vol. 29, no. 3, pp. 706–728, Jul. 2004.
- [17] D. R. Breese and G. Beauchage, "A review of modeling approaches for oriented semi-crystalline polymers," *Curr. Opin. Solid State Mater. Sci.*, vol. 8, no. 6, pp. 439–448, 2004.
- [18] R. Arridge and P. Barham, "A fibre composite model of drawn crystalline polymers," *Polymer*, vol. 19, no. 6, pp. 654–658, 1978.
- [19] Mitsubishi Gas Chemical Company, Inc., *NYLON-MXD6 Properties and Applications*, Tokyo, Japan: Mitsubishi Gas Chemical Co., Ltd., 2018.
- [20] A. M. A. M. Wahl, *Mechanical Springs*. Cleveland, OH, USA: Penton, 1944.
- [21] S. K. Fenster and A. C. Ugural, *Advanced Mechanics of Materials and Applied Elasticity*, 5th ed. London, U.K.: Pearson, 2011.
- [22] S. Kamarul Bahrain and J. Mahmud, "Tensile properties of silicone rubber via experimental and analytical method adapting hyperelastic constitutive models," *J. Eng. Appl. Sci.*, vol. 12, pp. 7703–7707, Dec. 2017.
- [23] G. Krishnan, "Kinematics of a new class of smart actuators for soft robots based on generalized pneumatic artificial muscles," in *Proc. IEEE/RSJ Int. Conf. Intell. Robots Syst.*, 2014, pp. 587–592.
- [24] S. M. Marco and W. L. Starkey, "A concept of fatigue damage," *Trans. Amer. Soc. Mech. Engineers*, vol. 76, pp. 627–632, Jul. 1954.
- [25] N. S. Nise, *Control Systems Engineering*, 5th ed. Hoboken, NJ, USA: Wiley, 2008.
- [26] M. Russo et al., "Continuum robots: An overview," *Adv. Intell. Syst.*, vol. 5, no. 5, 2023, Art. no. 2200367.
- [27] D. Bruder, X. Fu, R. B. Gillespie, C. D. Remy, and R. Vasudevan, "Koopman-based control of a soft continuum manipulator under variable loading conditions," *IEEE Robot. Automat. Lett.*, vol. 6, no. 4, pp. 6852–6859, Oct. 2021.
- [28] J. van der Weijde, B. Smit, M. Fritschi, C. van de Kamp, and H. Vallery, "Self-sensing of deflection, force, and temperature for joule-heated twisted and coiled polymer muscles via electrical impedance," *IEEE/ASME Trans. Mechatron.*, vol. 22, no. 3, pp. 1268–1275, Jun. 2017.



Brianna Ashcroft is currently working toward the undergraduate degree in mechanical engineering with Arizona State University (ASU), Tempe, AZ, USA.

She is also an Undergraduate Research Assistant with the Robotics Actuators and Dynamics Laboratory, ASU. Her research interests include soft actuators and robotics.



Phong Nguyen is currently working toward the undergraduate degree in mechanical engineering with Arizona State University (ASU), Tempe, AZ, USA.

He is also an Undergraduate Research Assistant with the Robotics Actuators and Dynamics Laboratory, ASU. His research interests include soft actuators and quadruped robots.



Jiefeng Sun (Member, IEEE) received the B.S. degree in mechanical engineering from the Lanzhou University of Technology, Lanzhou, China, in 2014, the M.S. degree in mechanical engineering from the Dalian University of Technology, Dalian, China, in 2017, and the Ph.D. degree in mechanical engineering from Colorado State University, Fort Collins, CO, USA, in 2022.

He is currently an Assistant Professor with Arizona State University (ASU), Tempe, AZ, USA, where he is also the Director of Robotic Actuators and Dynamics Lab. His research interests include artificial muscle, soft robots, wearable robots, and reconfigurable robots.



Eric Weissman received the B.S. degree in aerospace engineering in 2024 from Arizona State University, Tempe, AZ, USA, where he is currently working toward the Ph.D. degree in mechanical engineering.

His research interests include soft robotic actuators, compliant robotic systems, and quadrupedal robotics.